ORIGINAL PAPER

Initially rigid cohesive laws and fracture based on edge rotations

P. Areias · T. Rabczuk · P. P. Camanho

Abstract We propose alternative methods for performing FE-based computational fracture: a mixed mode extrinsic cohesive law and crack evolution by edge rotations and nodal reposition. Extrinsic plastic cohesive laws combined with the discrete version of equilibrium form a nonlinear complementarity problem. The complementarity conditions are smoothed with the Chen-Mangasarian replacement functions which naturally turn the cohesive forces into Lagrange multipliers. Results can be made as close as desired to the pristine strict complementarity case, at the cost of convergence radius. The smoothed problem is equivalent to a mixed formulation (with displacements and cohesive forces as unknowns). In terms of geometry, our recently proposed edge-based crack algorithm is adopted. Linear control is adopted to determine the displacement/load parameter. Classical benchmarks in computational fracture as well as newly proposed tests are used in assessment with accurate results. In this sense, the proposed solution has algorithmic and accuracy advantages, at a slight penalty in the computational cost. The Sutton crack path criterion is employed in a preliminary path determination stage.

Keywords Computational fracture · Extrinsic law · Complementarity · Edge rotation · Mixed-mode fracture

P. Areias (✉)
Physics Department, Colégio Luís António Verney, University of Évora, Rua Romão Ramalho, 597002-554 Evora, Portugal
e-mail: pmaa@uevora.pt

T. Rabczuk
Institute of Structural Mechanics, Bauhaus-University Weimar, Marienstraße 15, 99423 Weimar, Germany

P. P. Camanho
DEMEC Faculdade de Engenharia, Universidade do Porto, Rua Dr. Roberto Frias s/n, 4200-465 Porto, Portugal

1 Introduction

Two key topics are currently of interest in computational fracture with finite elements: the prediction and implementation of the crack path geometry and the cohesive law representation. For use with finite elements, crack propagation algorithms have been developed in the past two decades with varying degrees of accuracy and generality. Existing techniques can be classified as discrete or continuum-based (and are often a combinations of these):

- Full and localized rezoning and remeshing approaches [5, 11,16,24,49], variants of local displacement [30,33,36, 37,41–43] (or, in alternative, strain [2,40]) enrichments, clique overlaps [28], edges repositioning or edge-based fracture with R-adaptivity [35];
- Element erosion [48], smeared band procedures [39], viscous-regularized techniques [27], gradient and non-local continua [46];
- Phase-field models based on decoupled optimization (equilibrium/crack evolution) with sensitivity analysis [18].

For finite strain simulations, each one has particular advantages and shortcomings, most well documented. Notwithstanding, numerical experimentation is still essential for obtaining definitive conclusions. Specifically, the extended finite element method (XFEM) by Belytschko and co-workers [12,15,37] was used previously but still poses challenges for large amplitude displacements (this is particularly important for quasi-adiabatic shear bands). Densification of the Jacobian matrix occurs due to pile-up of degrees-of-freedom for nodes contributing to multiple cracks. If n_c cracks are present in elements in the support of a given node, this has $(1 + n_c)n_{SD}$ degrees of freedom where n_{SD} is the
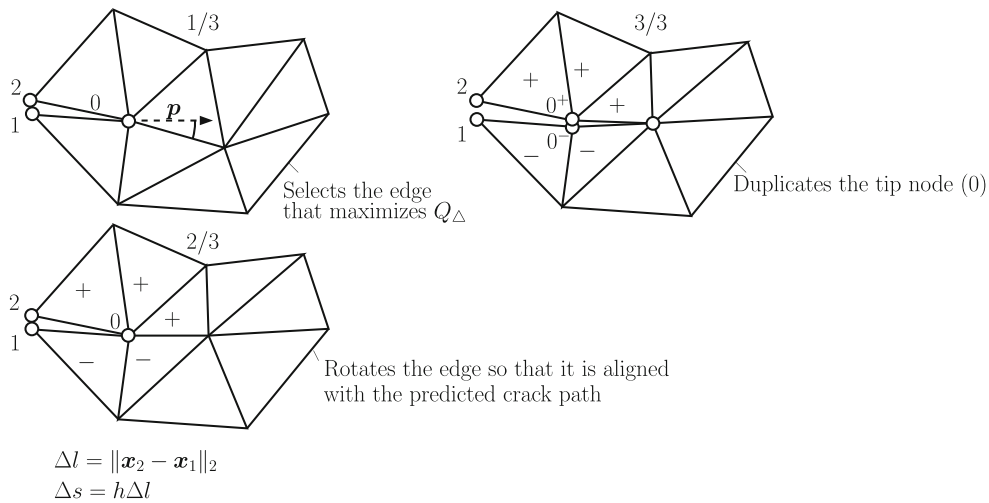
Fig. 1 Edge-based crack propagation algorithm in three steps. h is the plate thickness

number of original degrees-of-freedom per node; this produces a fill-in in the sparse Jacobian contrasting with remeshing that retains sparsity along the analysis. The adaptation of classical contact and cohesive techniques to deal with enriched elements is difficult. It is worth noting that large amplitude displacements are managed (see, e.g. [32]) by XFEM *if* neither contact nor cohesive forces are present. Difficulties in XFEM are often mitigated at the cost of intricate coding. As a consequence of these difficulties, typically idealized examples are displayed. Features are then added, such as crack face friction, coupled heat transfer, etc. From the enumerated options, it is often pointed out that local remeshing techniques lead to ill-formed elements (in particular blade and dagger-shaped triangles) which compromise the solution accuracy. These ill-formed elements motivate, besides other aspects, the use of full remeshing. Recently, we proposed a new methodology to attenuate this problem (cf. [5]). In the present work, we further simplify the solution by moving

Fig. 2 Effect of `tol` in the satisfaction of complementarity

edges so that they align with the predicted crack path. Its shell version found considerable success [9]. In this sense, the new proposal extends the idea of edge-based propagation established by Xie et al. [51]. In the present proposal, a quality indicator is used and fully finite-strain propagation is analyzed. Furthermore, consistent quasi-brittle fracture is considered and not only linear elastic fracture mechanics or, in the case of Xie and Gerstle [50], standard cohesive modeling.

Initially rigid cohesive laws with elastic unloading are cumbersome to implement and usually require a trust-region method (cf. [8]) to be employed for obtaining convergence. In addition, there is no clear underlying Mathematical support for the problem, in contrast with the plastic unloading cohesive case, which can be obtained by transforming the frictional contact problem. This has one advantage: if unloading is plastic or it does not occur, a problem similar to frictional contact can be solved and a cohesive-zone model is obtained.

The work is organized as follows: Sect. 2 presents the principle of virtual power for cracked bodies with cohesive regions, Sect. 3 shows the virtual crack closure technique for determination of energy release rate, the cohesive discretization and both the initiation and propagation algorithms. Section 4 presents six examples of fracture where comparisons with experimental results and alternative techniques are made. Finally, Sect. 5 reports the main conclusions
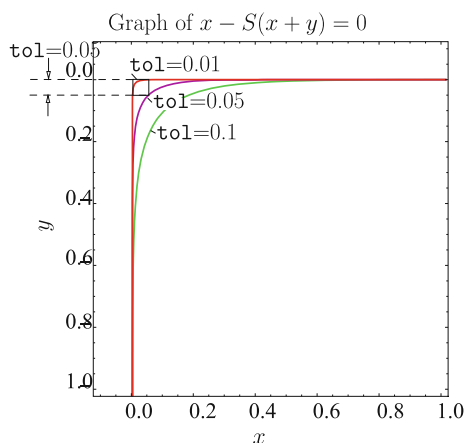
2 Principle of virtual power for cracked bodies with cohesive regions

Brittle and quasi-brittle fracture are differentiated by the geometry of the regions where energy dissipation occurs: in brittle fracture energy is dissipated in a crack edge or tip

and in quasi-brittle fracture energy is dissipated in a surface (typically identified as the cohesive surface). Since this cohesive surface must be formed as a consequence of a continuum condition, a continuous time path must be ensured. No energy release should occur by the single creation of cohesive surfaces, but rather by decohesion. We take a direct approach for dealing with equilibrium problems with cracks (both brittle and quasi-brittle). The formulation is based on the following approach:

- Explicitly including external loads and imposed velocities as well as the Lagrange multiplier for the brittle case.
- Including the cohesive zone Γ_c where the velocity jump is identified as $[[\dot{u}]]$. Note that part or whole of Γ_c may be unknown without consequences in the energy balance.
- Using a load parameter Q for proportional loading and a velocity parameter $\dot{q}$ for proportional imposed velocity:

$$\int_{\Omega} \sigma : \dot{\varepsilon} d\Omega = \int_{\Omega} Q b_\star \cdot \dot{u} d\Omega + \int_{\Gamma_t} Q t_\star \cdot \dot{u} d\Gamma_t \qquad (1)$$
$$+ \int_{\Gamma_u} \dot{q} t_u \cdot u_\star d\Gamma_u + \int_{\Gamma_c} t([[u]]) \cdot [[\dot{u}]] d\Gamma_c$$

where σ is the Cauchy stress tensor, $\dot{\varepsilon}$ is the strain rate, $b_\star$ is the nominal body force, $t_\star$ is the imposed surface load, t_u is the *reactive* surface traction and t is the cohesive traction. The unknown field is the displacement u and $u_\star$ is the nominal imposed displacement. Equation (1) has two interpretations: equivalence between internal and external power and, if the time derivative of displacement is interpreted as the virtual velocity, it is a form of the principle of virtual power with the required $\forall \dot{u}$ in the space of test functions. The subset of Γ_c where $[[u]] \neq 0$ is denoted Γ_{c_a} (the *active* cohesive zone). Energy is released by increasing of *both* the size of Γ_{c_a} and growth of $[[u]]$. For strictly closed cracks, $[[u]] \cdot t = 0$ on Γ_c, implying that t is a Lagrange multiplier (we now can use the notation t_λ) and the Eq. (1) is adapted to read:

$$\underbrace{\int_{\Omega} \sigma : \dot{\varepsilon} d\Omega}_{\dot{W}} = \underbrace{\int_{\Omega} Q b_\star \cdot \dot{u} d\Omega + \int_{\Gamma_t} Q t_\star \cdot \dot{u} d\Gamma_t + \int_{\Gamma_u} \dot{q} t \cdot u_\star d\Gamma_u}_{\dot{F}}$$
$$+ \underbrace{\int_{\Gamma_c} \left(t_\lambda \cdot [[\dot{u}]] + \dot{t}_\lambda \cdot [[u]] \right) d\Gamma_c}_{\dot{S}} \qquad (2)$$
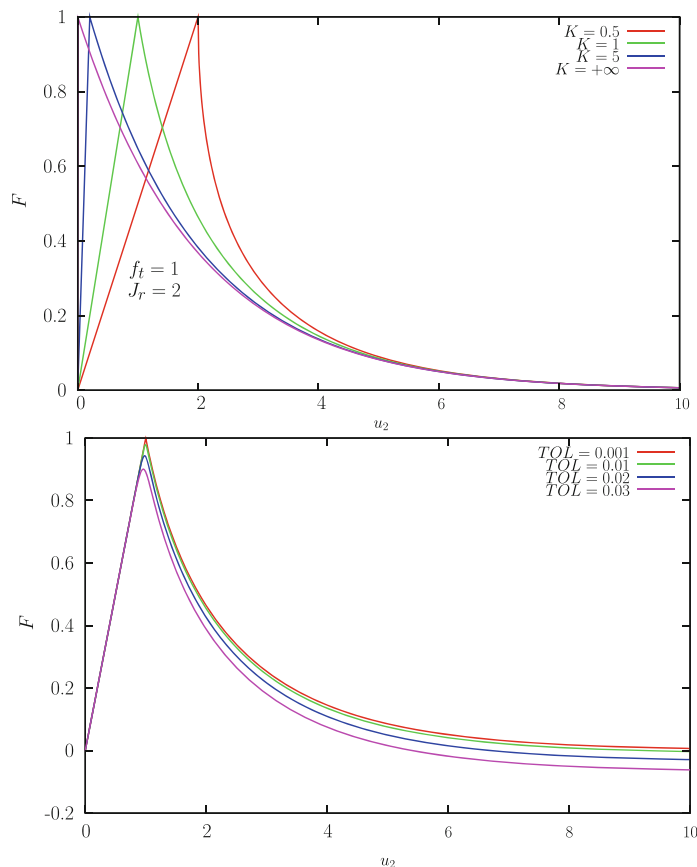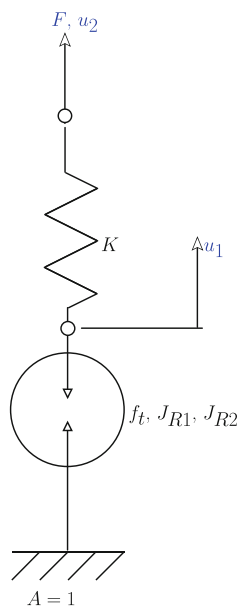

Fig. 3 1D model of the extrinsic cohesive law for mode-I. Effect of `tol` in the cohesive behavior

where t_λ is now an independent field at the crack faces, the Lagrange multiplier field conjugate to the constraint $[[u]] = 0$. Interpreting (1) and (2) as, respectively, the penalized and the Lagrange-multiplier versions of a constrained problem permits a unified treatment of brittle and quasi-brittle fracture. In (2) the energy is released by the increase of size of $\Gamma_{c_a} \subset \Gamma_c$, whereas in (1) energy is released by growth of Γ_{c_a}. We use s for the area of surface Γ_{c_a}. The strain work is calculated as:

$$W = \int_0^T \dot{W} \, dt \tag{3}$$

A classical switch of the derivatives from time t to area s results in:

$$\frac{dS}{ds} = \frac{dW}{ds} - \frac{dF}{ds} \tag{4}$$

where $S = \int_0^t \dot{S} d\tau$, $W = \int_0^t \dot{W} d\tau$ and $F = \int_0^t \dot{F} d\tau$ where $\dot{S}$, $\dot{W}$ and $\dot{F}$ are defined in Eq. (2), t is the time variable and τ is an integration variable. Standard arguments result in the following definition for the strain energy release, J:

$$J = -\frac{dS}{ds} = \frac{d(F - W)}{ds} \tag{5}$$

For elasto-plastic materials, we must acknowledge that part of the energy released from the crack advance was already dissipated by the plastic deformation process and therefore must be subtracted from the fracture energy:

$$J = J_R - W_p \Rightarrow \text{crack growth} \tag{6}$$

where J_R is the LEFM fracture energy (or critical energy release rate) for the considered material and geometry. In (6), W_p is the plastic deformation work, given as:

$$W_p = \int_0^T \sigma : \dot{\varepsilon}_p \, dt \tag{7}$$

where $\dot{\varepsilon}_p$ is the plastic strain rate. Finite element technology makes use of standard constant-strain triangles and isoparametric quadrilaterals, as well as our shell elements (cf. [7,10]).

3 Specific techniques for modeling crack growth

3.1 Virtual crack closure and crack advance

The determination of stress intensity factors can be performed by a variety of well-known methods all of which calculate the same configurational derivative (cf. [19]). The most established method is the contour J−integral. We have used contour integrals with success [49]. However, there are some shortcomings of J−integrals for multiple cracks and
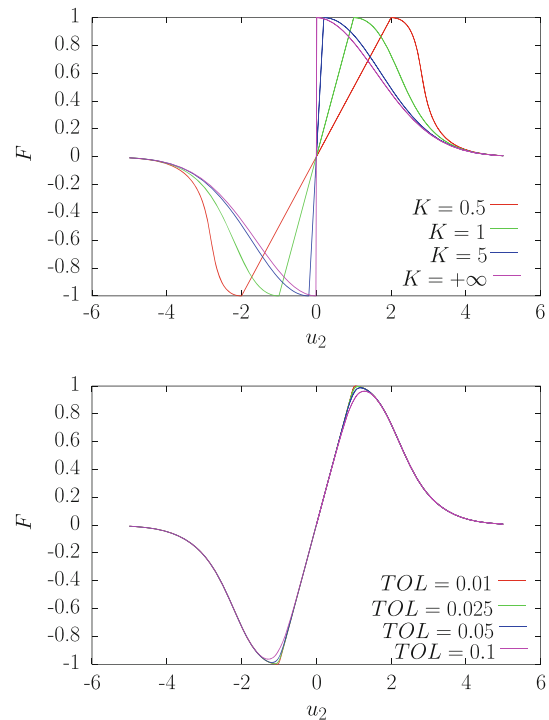

Fig. 4 1D model of the extrinsic cohesive law for mode-II. Effect of `tol` in the cohesive behavior
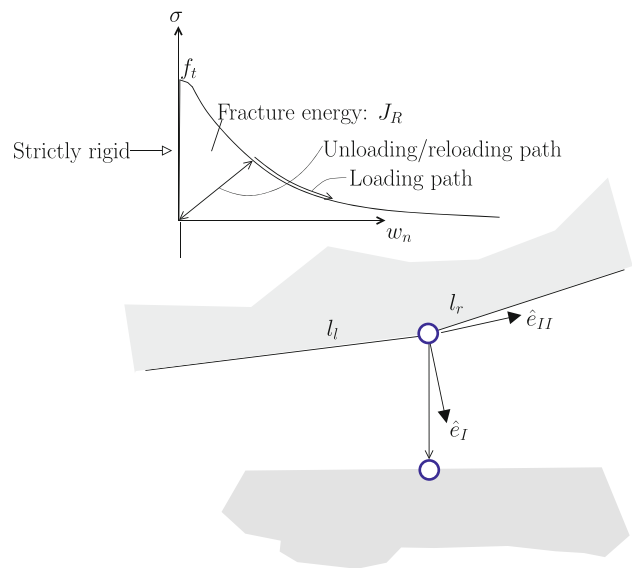

Fig. 5 Node-to-node cohesive element for finite displacements

the support function requires a user-defined radius. An alternative is the virtual crack closure technique (VCCT) created by Rybicki and Kanninen [44] and extensively reported by Krueger [31]. Furthermore, since it is based on the crack tip opening displacement (CTOD), it is known to have high predictive capabilities for large strain plasticity [34,47]. A short summary of the application of Krueger's approach is given here. Using a local frame corresponding to the classi-
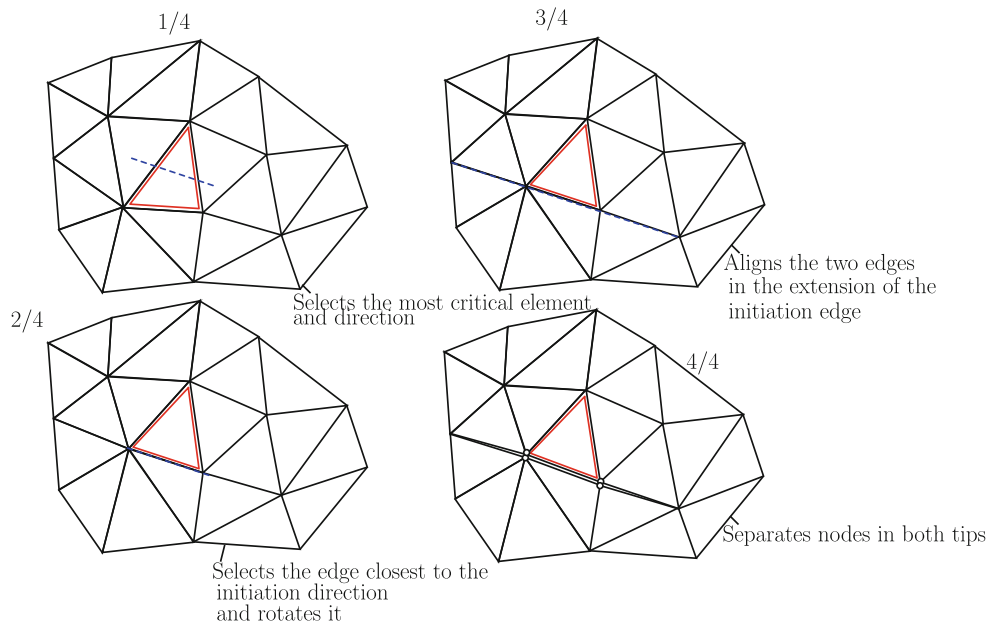
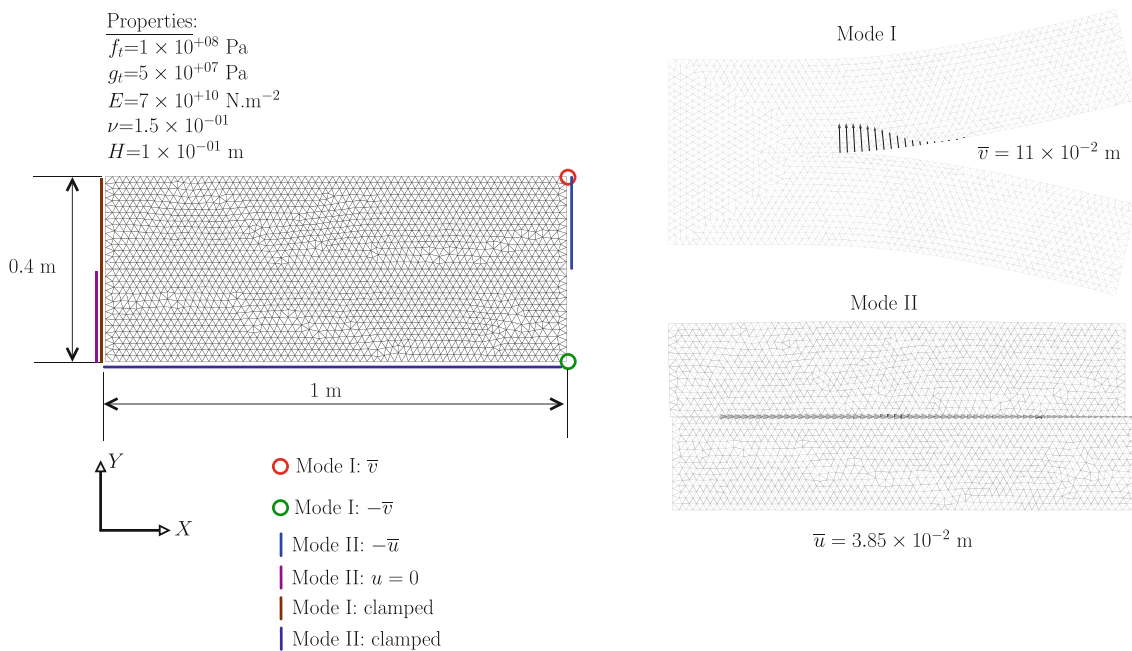**Fig. 6** Crack initiation based on edge rotation: 4 steps

Fig. 7 Verification test: relevant data for both tests. 2,129 nodes and 3,934 triangles are used

cal fracture mode decomposition (the mode frame), we can determine the transformation matrix whose rows are three orthogonal directions corresponding to each mode relative displacement:

$$
\boldsymbol{T}_{\text{mode}} = \begin{bmatrix} \hat{\boldsymbol{e}}_I^T \\ \hat{\boldsymbol{e}}_{II}^T \\ \hat{\boldsymbol{e}}_{III}^T \end{bmatrix} \tag{8}
$$

where

$$
\hat{\boldsymbol{e}}_{III} = \boldsymbol{n} \tag{9}
$$

with $\boldsymbol{n}$ being the normal unit vector, which in 2D is $\{0, 0, 1\}^T$. In addition,

$$
\boldsymbol{e}_{II}^\star = \left[\boldsymbol{x}_0 - \left(\frac{\boldsymbol{x}_1 + \boldsymbol{x}_2}{2} \right) \right] \tag{10}
$$

$$
\boldsymbol{e}_{II} = (\boldsymbol{I} - \boldsymbol{n} \otimes \boldsymbol{n}) \, \boldsymbol{e}_{II}^\star \tag{11}
$$
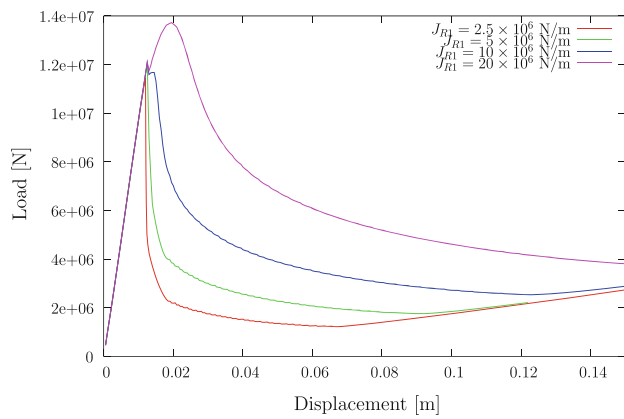
(a) Mode I, load/transversal displacement.
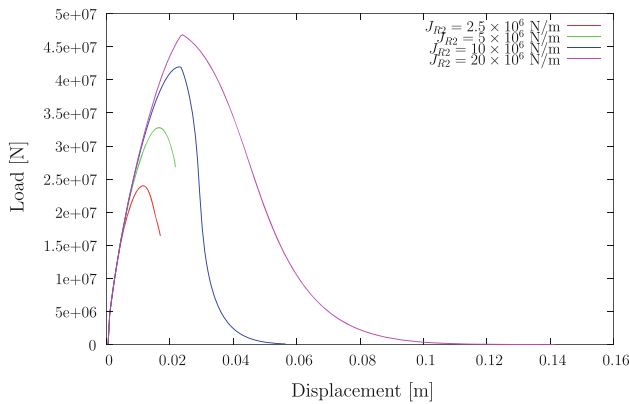
(b) Mode II, load/longitudinal displacement.

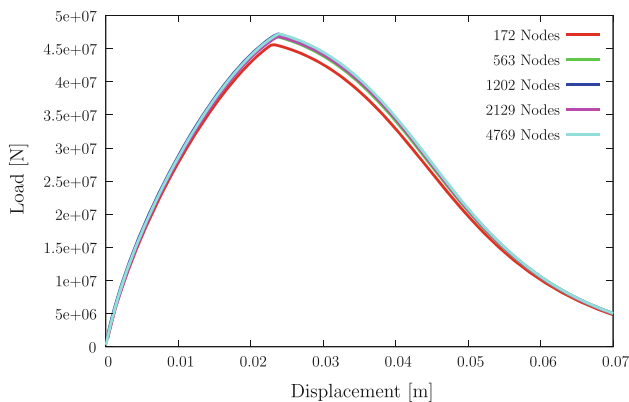**Fig. 8** Verification test: mode I and mode II results

Fig. 9 Mode II mesh sensitivity analysis

and $\hat{e}_I$ is given by

$$\hat{e}_I = \hat{e}_{III} \times \hat{e}_{II} \tag{12}$$

The classical notation for unit vectors using the Euclidian norm is adopted:

$$\hat{\bullet} = \frac{\bullet}{\| \bullet \|_2} \tag{13}$$

The relative displacement for the mode frame is given by:

$$\begin{Bmatrix} u_I \\ u_{II} \\ u_{III} \end{Bmatrix} = T_{\mathrm{mode}} \left(u_2 - u_1 \right) \tag{14}$$

and the internal forces at the tip are obtained by assembling elements above the predicted crack segment:

$$\begin{Bmatrix} f_I^+ \\ f_{II}^+ \\ f_{III}^+ \end{Bmatrix} = T_{\mathrm{mode}} f_{0i}^+ \tag{15}$$

where f_{0i}^+ are the internal forces assembled from elements identified as $+$ in Fig. 1 at the tip node (0).

Predicted fracture energies follow the classical derivation by Krueger (s identified in Fig. 1):

$$J_I = \frac{1}{2\Delta s} f_I^+ u_I \tag{16}$$

$$J_{II} = \frac{1}{2\Delta s} f_{II}^+ u_{II} \tag{17}$$

$$J_{III} = \frac{1}{2\Delta s} f_{III}^+ u_{III} \tag{18}$$

The condition for crack advance in brittle cases results from the energy sum corresponding to (6):

$$J_I + J_{II} + J_{III} = J_R \tag{19}$$

The crack path orientation follows our previous approach ([5]). For shells, the crack path has only components along $\hat{e}_I$ and $\hat{e}_{II}$ and the Ma-Sutton criterion [34,47] is adopted to predict it:

$$p = \hat{e}_1 \sin(\theta_c) + \hat{e}_2 \cos(\theta_c) \tag{20}$$

where the angle θ_c is obtained as:

$$\theta_c = \begin{cases} \frac{-36.5\pi}{180} \arctan(2.2\alpha), & |\alpha| < \alpha_c \\ \frac{57.3\pi}{180} \cos(\alpha) \frac{\alpha}{|\alpha|} & |\alpha| \geq \alpha_c \end{cases} \tag{21}$$

$\alpha = \arctan\left(\frac{u_{II}}{u_I}\right)$. For the cohesive fracture modeling, it is important to note that crack path is still determined by this analysis prior to the cohesive stage. For crack propagation, Fig. 1 illustrates the three main steps. In the first step a measure of the resulting triangle quality is used to compare the choices:

$$Q_\triangle = \frac{4\sqrt{3} A_\triangle}{l_1^2 + l_2^2 + l_3^2} \tag{22}$$

where $A_\triangle$ is the area of the triangle and l_1, l_2 and l_3 are the edge lengths of the triangle. This value is obtained by "trial" rotations of corresponding edges. In the second step the edge is rotated and history is mapped (a requirement for elastoplastic analysis, for example). Finally, in the third step the tip node is duplicated.
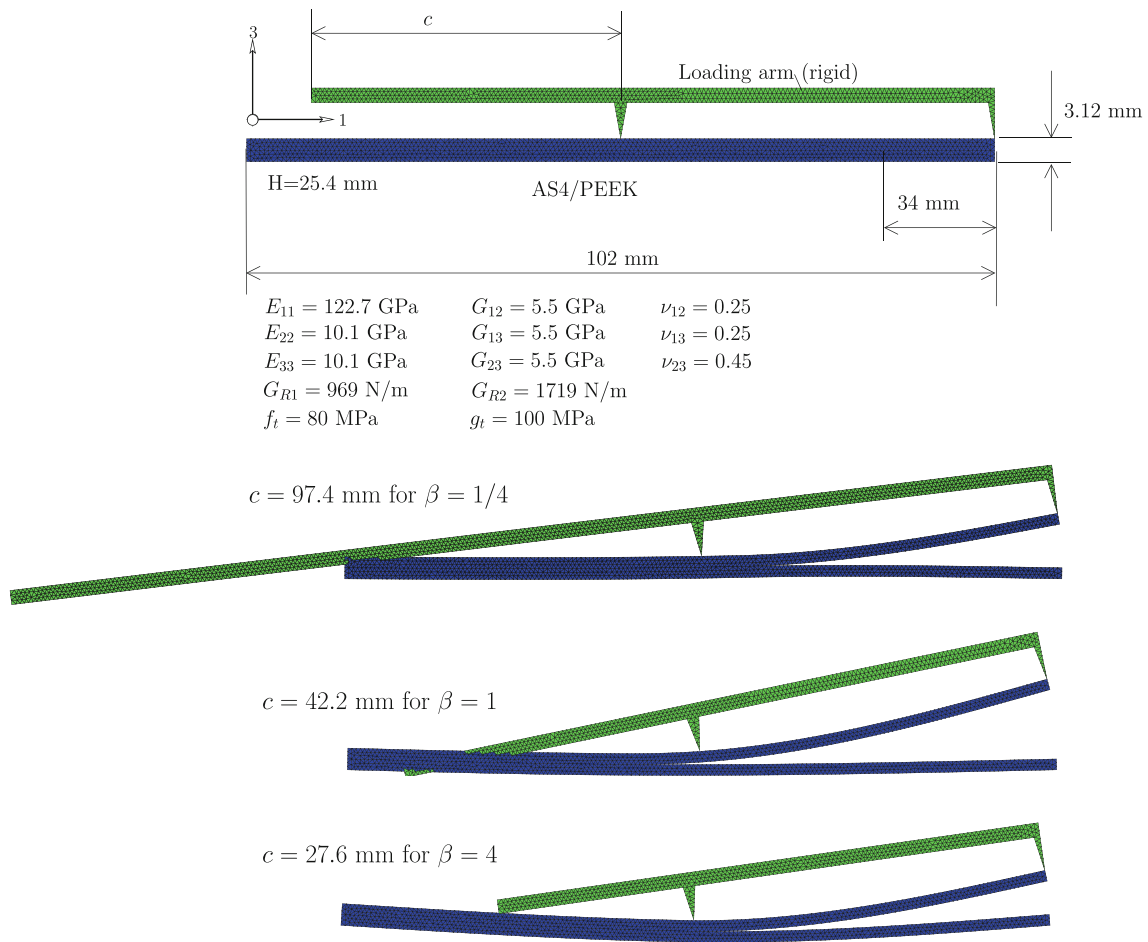
Fig. 10 Relevant data for the mixed-mode bending test as described by Camanho and Dávila. Also shown are the three cases of bending, $\beta = \frac{1}{4}$, $\beta = 1$ and $\beta = 4$
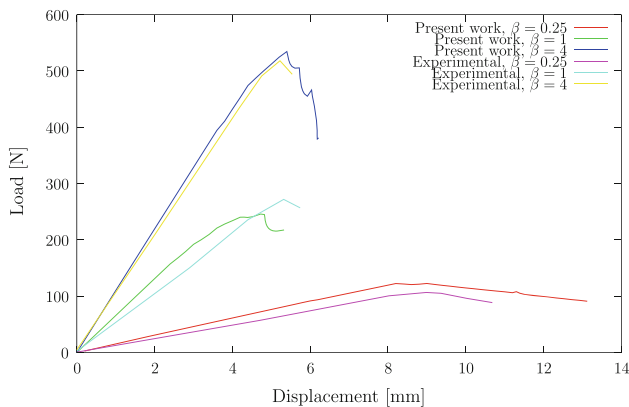

Fig. 11 Mixed-mode bending test: comparison with experimental results

3.2 Extrinsic traction separation law

The cohesive law is described by three complementarity conditions, one for the normal interaction and two for the tangential interaction. The normal interaction is a modification of

the normal contact conditions, written for the normal stress σ:

$$K \Delta u_n - \langle K \Delta u_n + \sigma^\star \rangle = 0 \tag{23}$$

$$\sigma = \sigma^\star + \Delta\sigma \tag{24}$$

$$\Delta u_n = [[u_n]] - \kappa \tag{25}$$

where K is a constant with units $[FL^{-3}]$ necessary for the unit consistency of (23). The stress difference $\Delta\sigma$ is given by:

$$\Delta\sigma = f_t \exp\left(-\frac{f_t}{J_{R1}} [[u_n]]\right) \tag{26}$$

with f_t being the cohesive tensile stress and J_{R1} the fracture energy in mode I. The term Δu_n is the difference between the normal displacement jump $[[u_n]]$ and the kinematic variable κ which is given as the maximum value of $[[u_n]]$ attained up to the current instant:
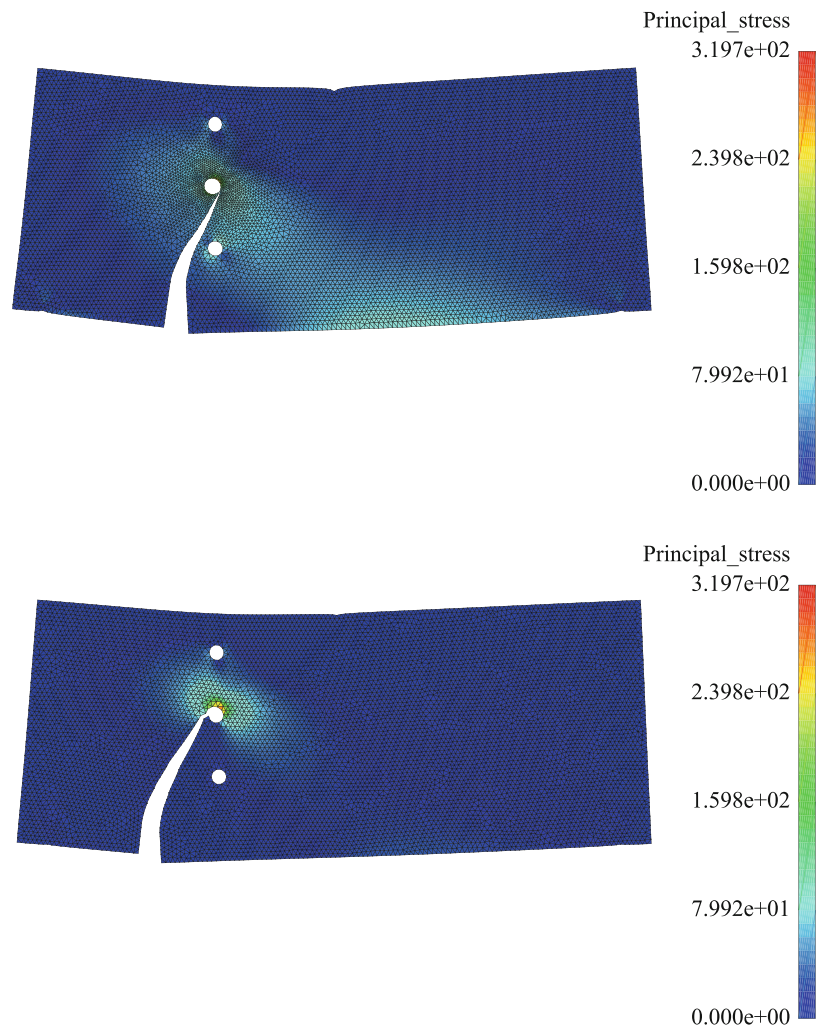
$$\kappa = \max_{\text{history}} [[u_n]] \tag{27}$$

The stress term $\sigma^\star$ is the contact stress in the absence of cohesive law (given by the difference $\Delta\sigma$). The step function

**Fig. 12** Bittencourt's drilled plate: geometry, boundary conditions and material properties. Geometry parameters a and b vary according to the specimen. Results shown for specimens #1 and #2
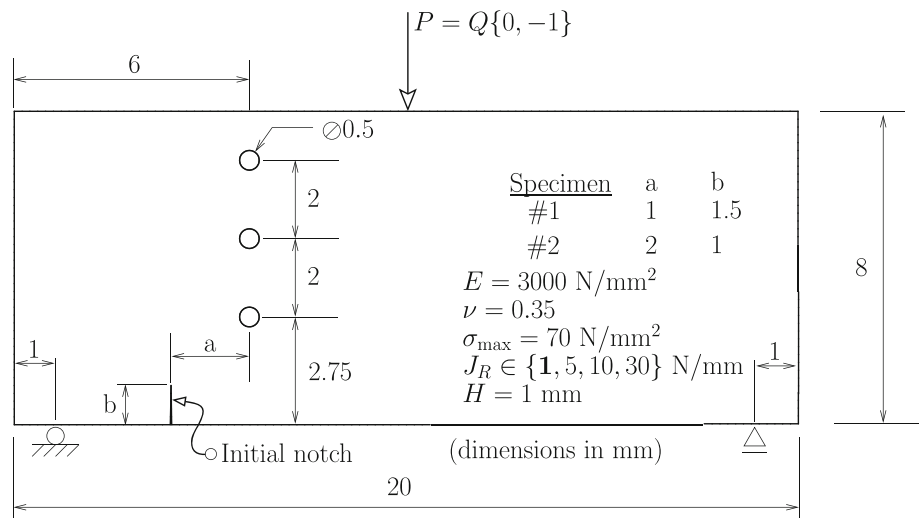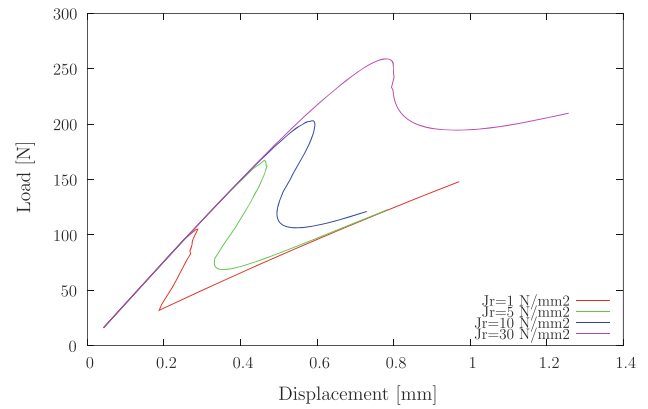

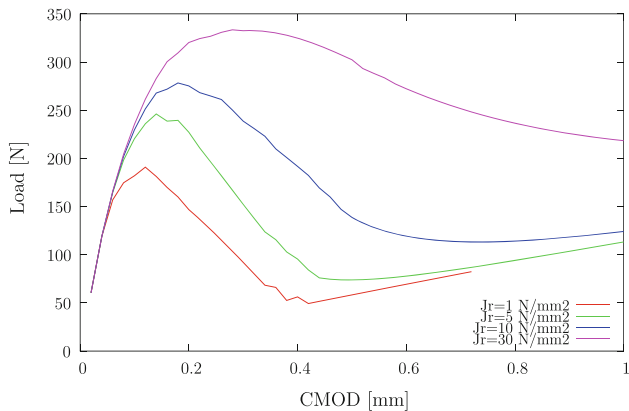(a) Relevant data for Bittencourt's drilled plate.

(b) Specimens #1 and #2 maximum principal stress over deformed meshes (without magnification). Specimen #1 contains 9126 initial nodes and Specimen #2 contains 8248 initial nodes.
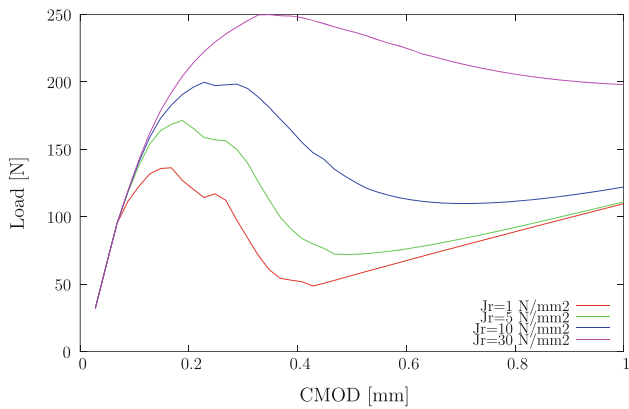
(a) Specimen #1

(a) Specimen #1

(b) Specimen #2
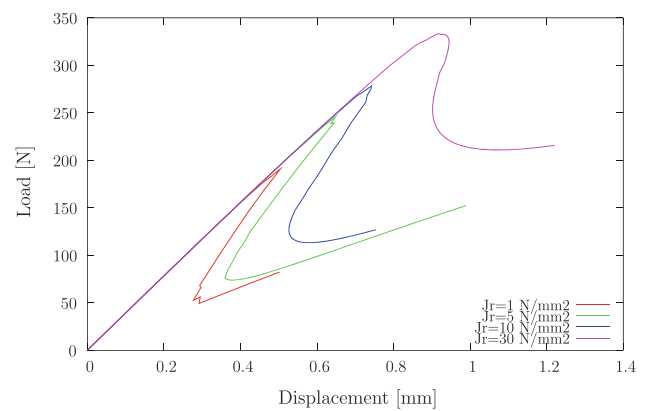
(b) Specimen #2

Fig. 13 CMOD/load results for the two specimens

Fig. 14 Displacement/load results for the two specimens

$< \bullet >$ in (25), using the Macaulay brackets is defined as:

$$< \bullet > := \frac{\bullet + |\bullet|}{2} \quad \bullet \in \mathbb{R} \tag{28}$$

For mode II, a related complementarity formulation is given by:

$$\phi_i - < \phi_i - K g_i > = 0$$

where $\phi_i = \Delta \tau + (-1)^i \tau$ and $g_1 = s$ and $g_2 = s - [[u_t]]$. τ is the effective shear stress, $\Delta \tau$ is the cohesive tangential stress and s is the tangential displacement shift. The tangential displacement jump $[[u_t]]$ is not affected by a history variable as was the case of the normal. The tangential cohesive law is given by:

Fig. 15 Specimen #1: cohesive tails for $J_R = 1, 5, 10, 30$ N/mm. Similar tails are obtained for specimen #2

$J_R = 1$ N/mm (and mesh)

$J_R = 10$ N/mm

$J_R = 5$ N/mm

$J_R = 30$ N/mm

CMOD=1.22 mm

Fig. 16 Crack path comparison with the results by Bittencourt et al. [16]
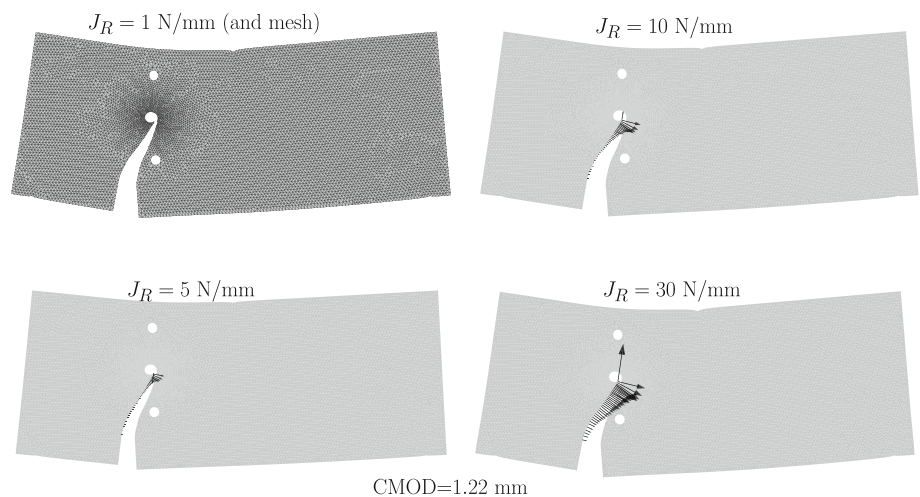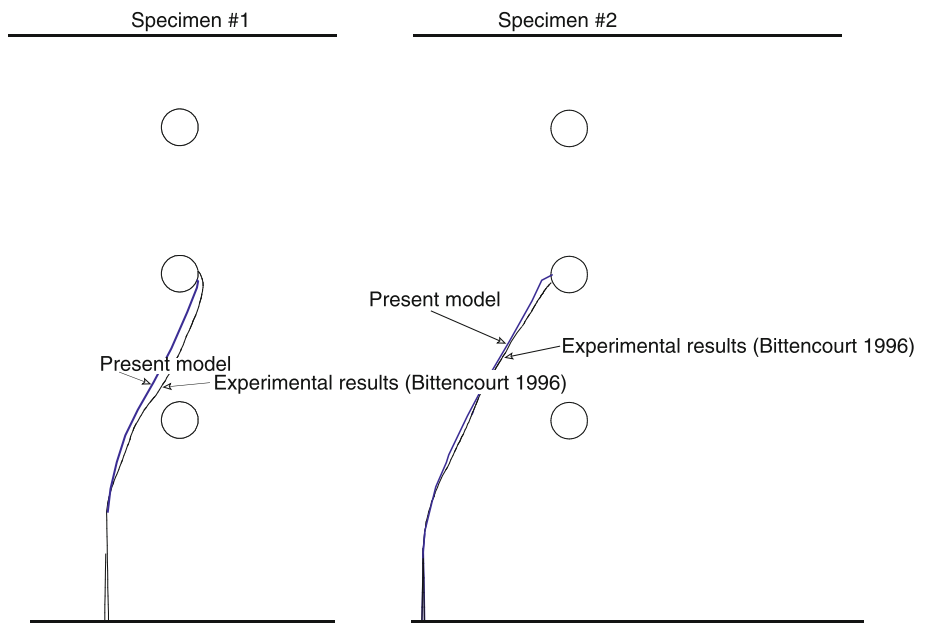

Specimen #1 — Specimen #2

Present model

Experimental results (Bittencourt 1996)

Present model

Experimental results (Bittencourt 1996)

$$\Delta \tau = g_t \exp\left(-\frac{g_t^2}{4 J_{R2}^2} [[u_t]]^2 \right) \tag{29}$$

where J_{R2} is the fracture energy in mode II and $g_t = \beta f_t$ is the maximum tangential stress. The reader can note that, if the Coulomb dry friction is considered, the cohesive tangential stress is then given by the following law:

$$\Delta \tau = \mu \sigma \tag{30}$$

where μ is the friction coefficient. Regularization of the step function makes use of the Chen-Mangasarian replacement function (cf. [22,23]) which is written as $< x > \cong S(x)$ with

$$< x > \cong S(x) = x + \frac{1}{\alpha} \log \left[1 + \exp\left(-\alpha x \right) \right] \tag{31}$$

with $\alpha = \log(2)/\texttt{tol}$. The effect of $\texttt{tol}$ in the complementarity satisfaction is shown in Fig. 2. Obviously, $\texttt{tol}$ is the vertical distance, represented in that Figure, between the origin and the "corner" point of the curve. For 3D problems, *cone-complementarity* must employed if a similar smoothing approach is to be used, as discussed for friction by Kanno et al. [29]. The mode-I model is represented in 1D in Fig. 3 as a spring/cohesive element in series. The effect of $\texttt{tol}$ in the Force/Displacement law is also shown in Fig. 3. Analogously, mode-II model is represented in 1D in Fig. 4. The cohesive traction t is obtained using the transformation matrix T_mode as:

$$t = T_\text{mode} \begin{Bmatrix} \sigma \\ \tau \\ 0 \end{Bmatrix} \tag{32}$$

Remarks:

- The Chen-Mangasarian approach introduces *one* additional degree-of-freedom in each exterior node for the normal force and *two* additional degrees-of-freedom for the tangential force and shift.
- The smoothing technique does not transform the problem into a barrier or penalty problem. It is akin to the second-order Lagrange multiplier approach for inequalities [38], but of course resulting in a fully differentiable (substitute) problem with additional degrees-of-freedom.
- All examples are solved with $\texttt{tol} = 1 \times 10^{-3} f_t$.
- K is determined as:

$$K = \frac{E}{5 \times 10^{-3} l_c} \tag{33}$$

where E is the arithmetic-averaged elasticity modulus and l_c is the average edge size in the mesh.

CMSD

E=35000 N/mm^2
ν=0.15
f_t=3.0 N/mm^2
J_R=0.1 N/mm
β=0.6
h=100 mm
(Dimensions are in mm)

20

80

$\frac{1}{11}$ Q

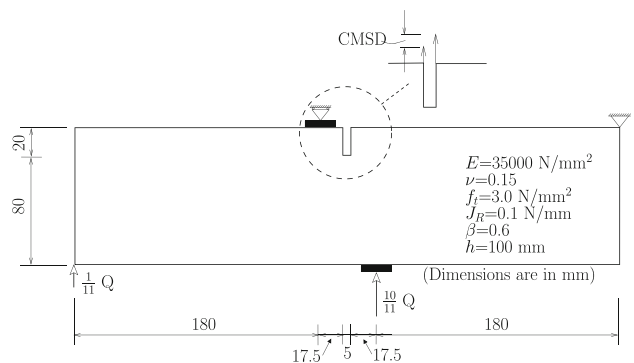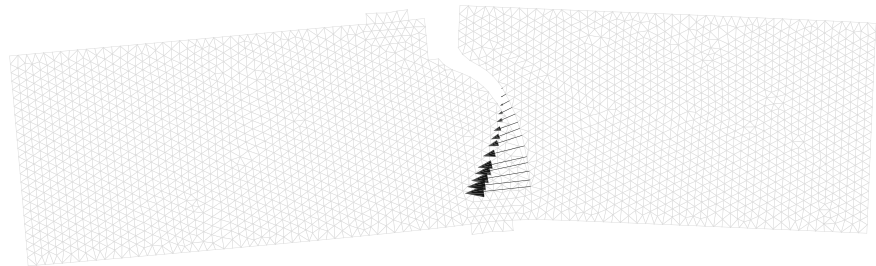$\frac{10}{11}$ Q

180

17.5 5 17.5

180

Fig. 17 Schlangen's SEN test: geometry, boundary conditions and material properties

Fig. 18 Schlangen's SEN test: Deformed meshes for the three cases are shown, with 5616, 10014 and 22498 elements. Crack path (10,014 elements) compared with DSDA [25] (yellow) and the experimental results by Schlangen [45]

(a) 2939 nodes and 5616 elements (100× magnified). Normal cohesive stress is represented.
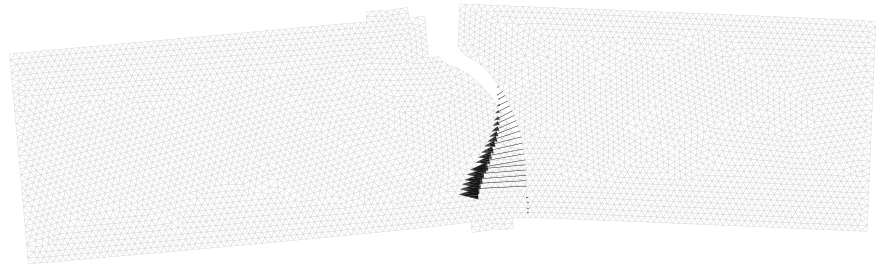
(b) 5185 nodes and 10014 elements (100× magnified). Normal cohesive stress is represented.
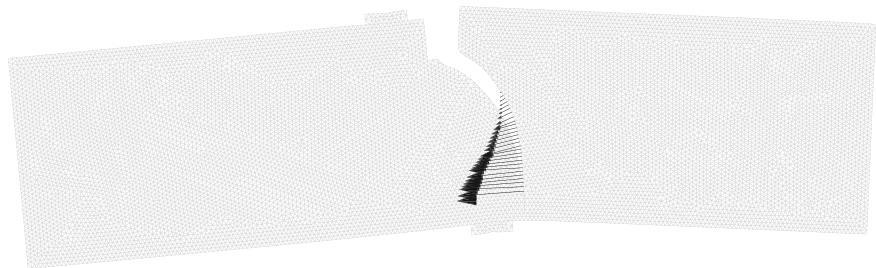
(c) 11514 nodes and 22498 elements (100× magnified). Normal cohesive stress is represented.

Experimental envelope (Schlangen 1993)

Present model

DSDA
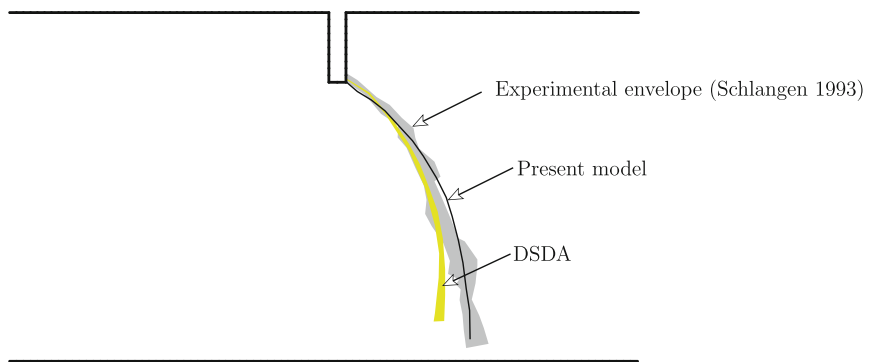
(d) Crack path comparison

3.3 Cohesive discretization

The representation of the finite-displacement cohesive element makes use of a simple node/node arrangement as depicted in Fig. 5. This approach is simpler than the node/edge method and it is sufficient for our purposes here where only moderate displacements are present. In addition, the surface Patch test is satisfied. We consider all external
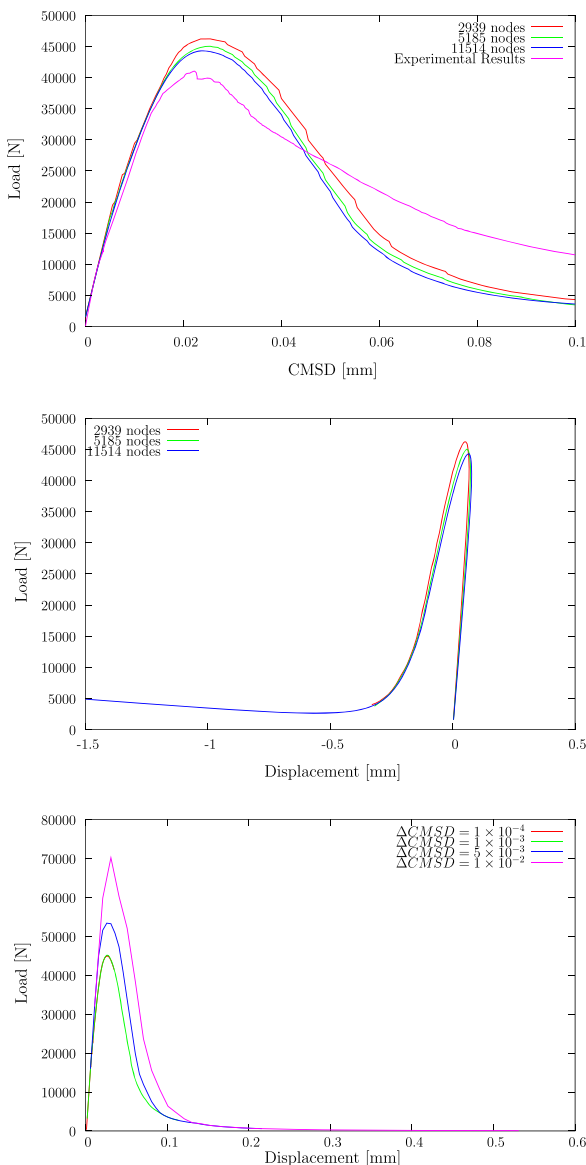
Fig. 19 Schlangen's SEN test: load-CMSD results: comparison with the experimental results by Schlangen [45] and the DSDA technique [25]. The effect of step-size ($\Delta CMSD$) in the results is also shown

edges (i.e. with only one underlying solid element) as candidates.

3.4 Crack initiation

For completeness, we show the crack initiation algorithm. Crack initiation occurs by satisfaction of a criterion at the continuum level. For damage-based constitutive laws, the damage or void fraction value are typically used. When strain softening is prone to occur, loss of strong ellipticity is also an acceptable criterion (cf. [10]). For many engineering materials, the only available information is the fracture strain, which depends on the tensile specimen geometry. Geometrically,

we maintain the edge-based approach as illustrated by Fig. 6. The steps are: first find the most critical element in terms of initiation criterion and the direction. Second, finds the edge with the minimum angle with respect to the predicted direction and rotates it. Third, aligns the edges that best extend the initiation edge and rotates them. Fourth, duplicates both tip nodes so that a three-edge crack appears.

This geometrical approach is very simple to implement and fits the subsequent propagation algorithm. Since no element subdivision occurs, the well known spurious element slicing is avoided. As a shortcoming, often there is some local mesh distortion, in particular with quadrilaterals.

3.5 Constraint-based solution control

For the determination of the load (or displacement) factor Q introduced in Sect. 2 either the energy release rate or the stress is constrained. An indirect form of achieving this is to control the CMOD (crack mouth opening displacement) or CMSD (crack mouth shear displacement). A complete discussion of the solution constraint is given in Moës and Belytschko [36] and an analogous procedure was described by Areias et al. [5]. If a load factor Q is included as an unknown, the system must be enlarged by appending the control constraint $s_c(\boldsymbol{u}) = 0$:

$$\boldsymbol{r}(Q, \boldsymbol{u}) = \boldsymbol{0} \tag{34}$$

$$s_c(\boldsymbol{u}) = 0 \tag{35}$$

where $\boldsymbol{r}(Q, \boldsymbol{u})$ is the discrete equilibrium residual and $s_c(\boldsymbol{u})$ is the crack constraint. For proportional loading and we can write $\boldsymbol{r}(Q, \boldsymbol{u})$ as:

$$\boldsymbol{r}(Q, \boldsymbol{u}) = Q\boldsymbol{e} - \boldsymbol{i}(\boldsymbol{u}) \tag{36}$$

with, following classical notation, $\boldsymbol{e}$ is the total load vector and $\boldsymbol{i}$ is the internal force vector. Generalizations of (36) are straightforward but for the present applications appear unnecessary. The solution by Newton-Raphson iteration results in:

$$\begin{bmatrix} \boldsymbol{K}(Q, \boldsymbol{u}) & -\boldsymbol{e}(Q, \boldsymbol{u}) \\ \boldsymbol{l}(\boldsymbol{u}) & 0 \end{bmatrix} \begin{Bmatrix} \boldsymbol{u}_v \\ Q \end{Bmatrix} = - \begin{Bmatrix} \boldsymbol{i}(\boldsymbol{u}) \\ s_c(\boldsymbol{u}) \end{Bmatrix} \tag{37}$$

where $\boldsymbol{u}_v$ is the iterative correction to the displacement $\boldsymbol{u}$ and the load factor. In (37), the quantities $\boldsymbol{l}$ and $\boldsymbol{K}$ are the following derivatives:

$$\boldsymbol{l}(\boldsymbol{u}) = \frac{\mathrm{d}s_c}{\mathrm{d}\boldsymbol{u}} \tag{38}$$

$$\boldsymbol{K}(Q, \boldsymbol{u}) = \frac{\partial \boldsymbol{i}(Q, \boldsymbol{u})}{\partial \boldsymbol{u}} \tag{39}$$

Defining $\boldsymbol{u}_i = \boldsymbol{K}^{-1}\boldsymbol{i}$ and $\boldsymbol{u}_e = \boldsymbol{K}^{-1}\boldsymbol{e}$, and subsequently $s_i = \boldsymbol{l} \cdot \boldsymbol{u}_i$, $s_e = \boldsymbol{l} \cdot \boldsymbol{u}_e$ we finally obtain:

Fig. 20 Gravity dam geometry and relevant data. Crack path comparison with the results from Barpi and Valente [14]

Properties #1:
$\overline{H=3 \times 10^{-01} \text{ m}}$
$f_c = 1.84 \times 10^{+02}$
$g_y = -9.8 \times 10^{+00} \text{ m.s}^{-2}$
$E = 3.57 \times 10^{10} \text{ N.m}^{-2}$
$\nu = 1 \times 10^{-01}$
$\rho_0 = 2.4 \times 10^{+03} \text{ Kg.m}^{-3}$

Properties #2:
$\overline{\text{Nominal x-pressure}} = -1.9608 \times 10^{-01} \text{ N.m}^{-2}$
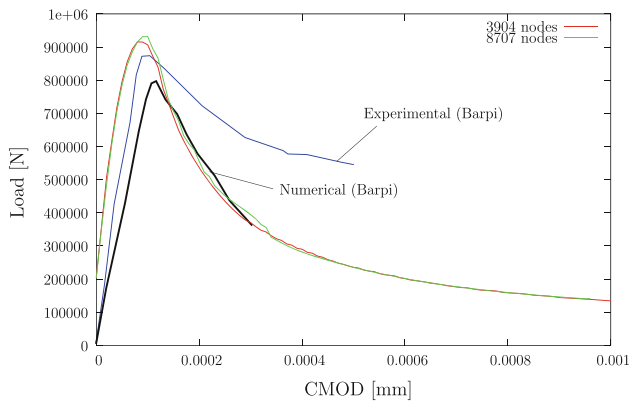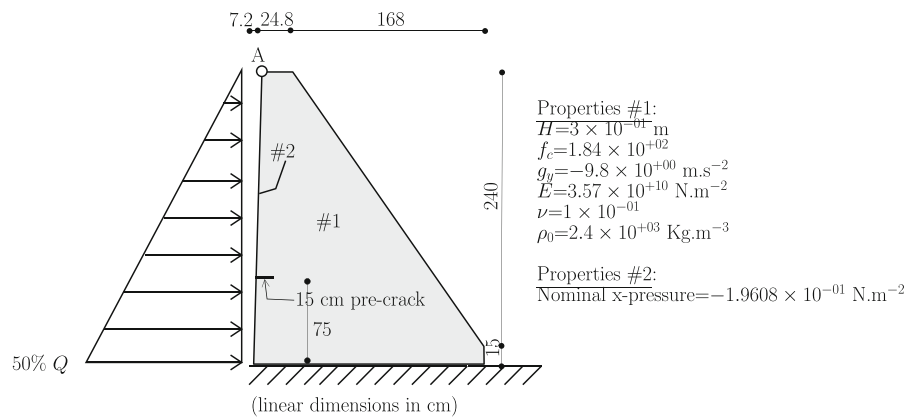
(linear dimensions in cm)

Fig. 21 Gravity dam CMOD/load results. A comparison with the results reported by Barpi and Valente is shown

$$Q = \frac{s_i - s_c}{s_e} \tag{40}$$

$$u_v = Q u_e - u_i \tag{41}$$

which provides the overall solution process for the constrained equilibrium. Of course, this procedure corresponds to an exact linearization if l is calculated in closed-form.

4 Computational fracture examples

Six sets of bi-dimensional fracture problems are solved. Assessment makes use of comparisons with experiments found in the literature and with alternative formulations. Step-size and mesh-size effects are also inspected. SIMPLAS software [3] is used.

4.1 Verification test

A demanding finite-strain numerical test for the cohesive law in mode I and mode II contexts is established. The initial "debonding" effect for small energies was found to be problematic in regularized, or intrinsic, cohesive laws, but is solved without difficulties by our complementary approach. This applies to both mode I and mode II tests. Geometry, boundary conditions and elastic properties are presented in Fig. 7. Artificially large peak stresses are used with the purpose of inspecting the finite strain behavior in terms of convergence and overall robustness. Results for modes I and II are shown in Fig. 8 as functions of J_{R1} and J_{R2}. Note that low values of J_R do not pose difficulties. Inspection of Fig. 8a, b allows the conclusion that this approach is able to capture sharp softening. For mode II and $J_{R2} = 20 \times 10^6 \text{ Nm}^{-1}$ a mesh convergence study is performed: meshes with $172, 563, 1202, 2129$ and 4769 nodes are compared in Fig. 8. Other cases are omitted since the conclusion is not altered: the present approach is very mesh-size insensitive. This result stems from careful coding and a complementarity-based approach (see also Fig. 9).

4.2 Mixed-mode bending test

We use a simple mixed mode numerical experiment to assess the robustness of the proposed smoothed complementarity approach for large values of displacement and cohesive forces. We consider the mixed-mode bending (MMB) test as discussed by Camanho and Dá vila (cf. [20,21]). These Authors have experimental data so that a comparison is made here. An AS4/PEEK composite is used in the test. Relevant data for this anisotropic test is shown in Fig. 10. Results are relatively close to the experiments, as depicted in Fig. 11. For conciseness, we refer to the work of Camanho [20,21] for further details concerning this problem. We note that, contrary to that work, the lever is here explicitly represented. In addition, no effort was made in "tuning" our methodology for composites.

4.3 Bittencourt's drilled plate (mode I)

We use the problem by Bittencourt et al. [16] who performed experimental and numerical studies of curvilinear crack propagation. Specimens are built of Polymethylmethacrylate (PMMA) and for this material, the inclusion of finite strains is important. The relevant geometry, material properties and

Fig. 22 Gravity dam. Principal stress contour plots and cohesive tails (×100 magnified)
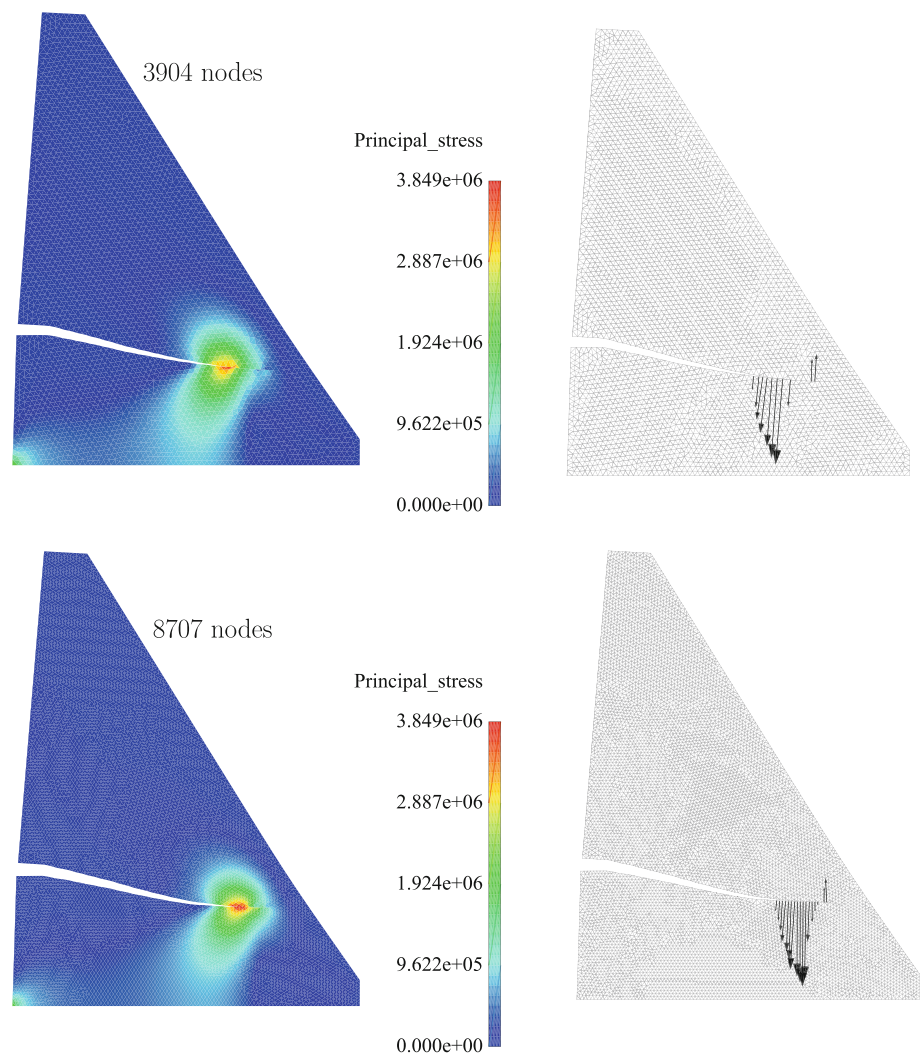
boundary conditions are shown in Fig. 12 for two specimens that differ in the linear dimensions *a* and *b*. In the paper by Bittencourt et al. [16], the Erdogan and Sih [26] fracture criterion was used, with stress intensity factors calculated with the domain-integral (see also [36] for a detailed discussion of this approach) and quarter-point elements. A recursive spatial decomposition method was introduced to perform the mesh subdivision. In the present approach, only specimen #1 required smaller elements when the coarser mesh was used (which was also a conclusion of Bittencourt et al.) in the crack turning region near the second hole. The presence of the three holes affects the stress field making the crack trajectory very sensitive to the position and size of the existent notch. Good agreement was observed between predicted and experimental crack paths (see Fig. 16). The crack mouth opening displacement (CMOD) is used to control the solution and capture the snap-backs. Load-CMOD results are shown in Fig. 13 for both specimens and load-deflection results are shown in Fig. 14, showing the well-known snap-backs. Smooth results

are obtained and we reach small fracture energies without convergence problems. For the four distinct values of the fracture energy the cohesive stresses are shown in Fig. 15.

4.4 Single edge notched beam

Now we analyze the single edge notched (SEN) beam introduced by Schlangen (cf. [45]). A description of this problem, with material properties and boundary conditions is presented in Fig. 17. Besides the classical analysis, we also inspect unloading and reloading behavior with the present plastic cohesive law. Three uniform triangular meshes with different densities are adopted. The arc-length method (see Sect. 3.5) is used, with monotonically increasing CMSD (crack mouth sliding displacement). The crack path reproduces closely the experimental envelope, as can be observed in Fig. 18; even near the support the experimental observations are accurately reproduced. A comparison with the experimental results and the DSDA method [1,4], along with
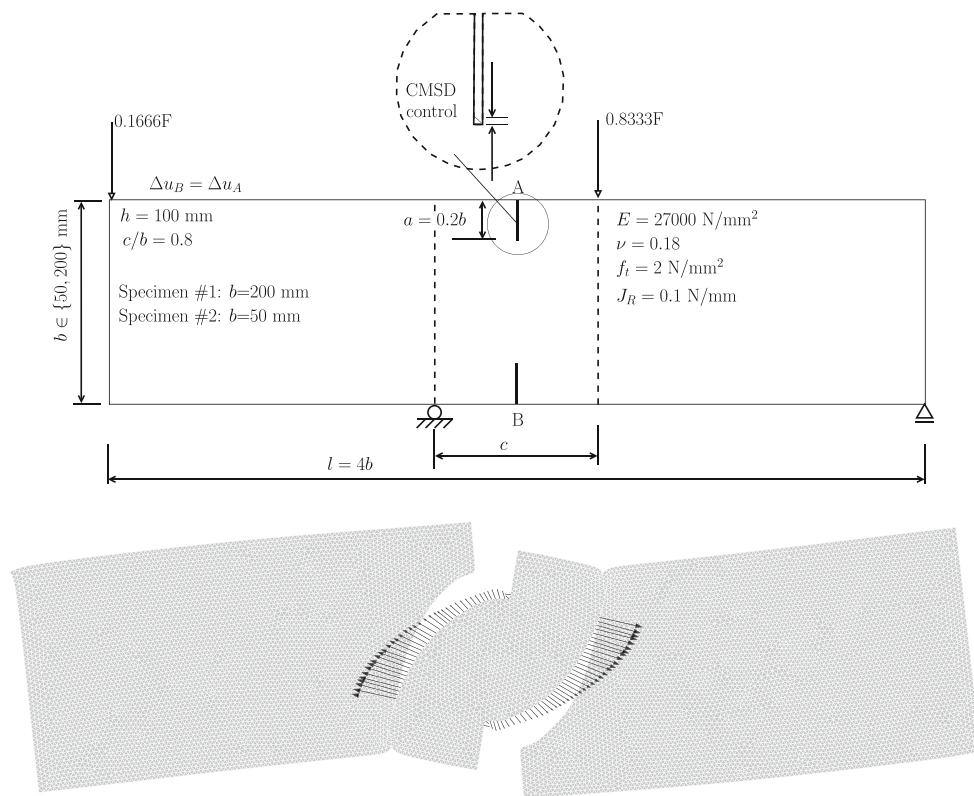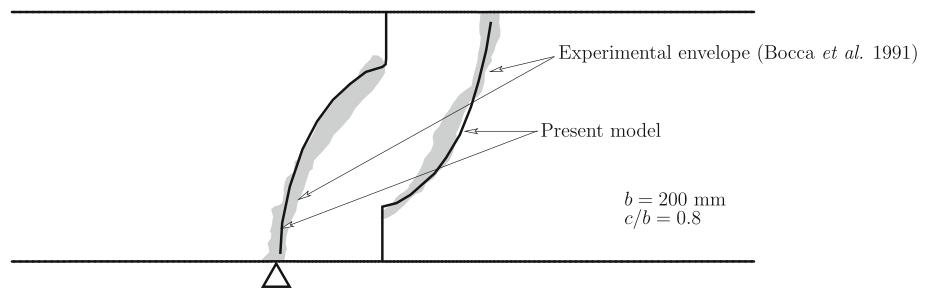
Fig. 23 Four-point bending of a concrete beam: geometry, boundary conditions, multipoint constraints ($\Delta u_B = \Delta u_A$) and material properties. Also shown is the final deformed mesh ×50 magnified with the attached cohesive stress vectors

Fig. 24 Four-point bending of a concrete beam: crack paths compared with the envelope of experimental results by Bocca et al. [17]

a study of mesh and step size influence is effected. As can be observed in Fig. 19, after the peak load is reached, the numerical results are more brittle than the experimental results. According to [2], this is due to the fact that an isotropic mode-I traction-jump law is used. The effect of the CMSD increments in the results is shown in the same Figure. The results are immune to the step-size up to very large CMSD increments (1×10^{-3}).

4.5 Gravity dam scale model

This problem is one of the scale model dam problems solved (and tested) by Barpi and Valente (cf. [14]). We use a 150 mm pre-crack in a model dam with the scale 1 : 40 as described

in that reference (note that there is also a specimen with a 300 mm pre-crack). A hydrostatic load is applied to the left face of the dam and self-weight is considered (this is replaced by a set of forces in the original work). Figure 20 presents the geometry, dimensions, loading and properties defining this problem. Also shown is a comparison with both experimental and numerical crack trajectories reported by Barpi and Valente. Two meshes are used (composed solely of triangles) containing 3,904 nodes and 8,707 nodes. The latter has a better agreement with the experimental crack path, as can be observed in Fig. 20. We also show the CMOD/load results compared with the ones reported by Barpi and Valente (Fig. 21). Cohesive tails and principal normal stresses are shown for the two meshes in Fig. 22.
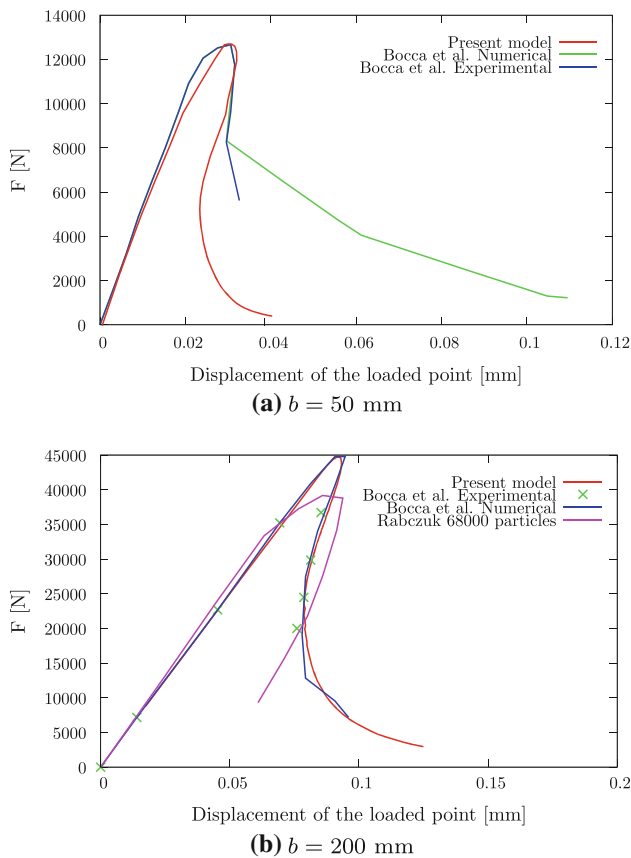
Fig. 25 Load-displacement results, compared with the results of Bocca et al. [17] and the cracking particle method of Rabczuk and Belytschko [43] (for the case $b = 200$ mm) with their 68,000 particle analysis

4.6 Cohesive crack growth in a four-point bending concrete beam

The four-point bending concrete beam problem consists of a bi-notched concrete beam subjected to two point loads. It was presented by Bocca et al. [17] and numerically tested by several authors. The effect of size is apparent since two specimens with different dimensions are tested. In the original work [17], the experimental setting is described in detail, being here omitted. From the set of specimens studied by Bocca et al. we only make use of the specimens with $c/b = 0.8$, $b = 50$ and $b = 200$ mm, since these have useful experimental data. We are concerned with the crack paths that were reported in [17]. Using the well-known cracking particle method, Rabczuk and Belytschko [43] obtained excellent results for the crack path prediction, although the load in the load-displacement diagram was somewhat higher than the experimental one. In addition, with the particle methods, there is the problem of selecting the support dimension in the crack region. We here use a single *uniform* mesh, with 11,599 nodes and 22,656 triangular elements. All relevant data is shown in Fig. 23. For anti-symmetry reasons, we

force the same mouth horizontal displacement at the edge of notches A and B: $\Delta u_B = \Delta u_A$. We obtain good agreement with the experimental crack paths, as shown in Fig. 24. The relatively wide spread of experimental crack paths is typical and results from the use of 6 specimens of reference [17]. Experimentally, some residual crack evolution in the opposite direction of the final path was observed and we also obtained that effect. Load-displacement results are shown in Fig. 25 where a comparison with the measurements of Bocca et al. [17] and the cracking particle method of Rabczuk and Belytschko [43] is made.

5 Conclusions

The simple algorithm of edge rotation for computational fracture combined with the extrinsic cohesive law provide an advantageous alternative to the tip remeshing algorithm proposed by the Authors (cf. [5–7,11,13]) and it is more convenient than enrichment techniques. Crack paths are more regular, Newton-Raphson convergence is better and less mesh distortion occurs. We found that both for brittle and quasi-brittle, classical benchmarks perform at least as well as alternative techniques. Recent enrichment techniques also show remarkable accuracy, but are more limiting for large amplitude displacements and the application to elasto-plastic problems is not clear. A subsequent manuscript is in preparation, applying the present algorithm to full 3D computational fracture.

References

1. Alfaiate J, Simone A, Sluys LJ (2003) A new approach to strong embedded discontinuities. In: Bicanic N, de Borst R, Mang H, Meschke G (eds) Computational modelling of concrete structures, EURO-C 2003, St. Johann im Pongau, Salzburger Land
2. Alfaiate J, Wells GN, Sluys LJ (2002) On the use of embedded discontinuity elements with crack path continuity for mode-I and mixed-mode fracture. Eng Fract Mech 69:661–686
3. Areias P Simplas. https://ssm7.ae.illinois.edu:80/simplas. Accessed 4 April 2013
4. Areias P, César de Sá JMA, Conceição António CA, Carneiro JASAO, Teixeira VMP (2004) Strong displacement discontinuities and Lagrange multipliers in the analysis of finite displacement fracture problems. Comput Mech 35:54–71
5. Areias P, Dias-da-Costa D, Alfaiate J, Júlio E (2009) Arbitrary bi-dimensional finite strain cohesive crack propagation. Comput Mech 45(1):61–75
6. Areias P, Dias-da Costa D, Pires EB, Infante Barbosa J (2012) A new semi-implicit formulation for multiple-surface flow rules in multiplicative plasticity. Comput Mech 49:545–564

7. Areias P, Garção J, Pires EB, Infante Barbosa J (2011) Exact corotational shell for finite strains and fracture. Comput Mech 48:385–406

8. Areias P, Rabczuk T (2007) Quasi-static crack propagation in plane and plate structures using set-valued traction-separation laws. Int J Numer Method Eng 74(3):475–505

9. Areias P, Rabczuk T (2013) Finite strain fracture of plates and shells with configurational forces and edge rotations. Int J Numer Method Eng, (in press)

10. Areias P, Ritto-Corrêa M, Martins JAC (2010) Finite strain plasticity, the stress condition and a complete shell model. Comput Mech 45:189–209

11. Areias P, Silva HG, Van Goethem N, Bezzeghoud M (2012) Damage-based fracture with electro-magnetic coupling. Comput Mech. doi:10.1007/s00466-012-0742-6

12. Areias P, Song JH, Belytschko T (2006) Analysis of fracture in thin shells by overlapping paired elements. Comp Method Appl M 195(41–43):5343–5360

13. Areias P, Van Goethem N, Pires EB (2011) A damage model for ductile crack initiation and propagation. Comput Mech 47(6):641–656

14. Barpi F, Valente S (2000) Numerical simulation of prenotched gravity dam models. J Eng Mech ASCE 126(6):611–619

15. Belytschko T, Black T (1999) Elastic crack growth in finite elements with minimal remeshing. Int J Numer Method Eng 45:601–620

16. Bittencourt TN, Ingraffea AR, Wawrzynek PA, Sousa JL (1996) Quasi-automatic simulation of crack propagation for 2D LEFM problems. Eng Fract Mech 55(2):321–334

17. Bocca P, Carpinteri A, Valente S (1991) Mixed mode fracture of concrete. Int J Solids Struct 27(9):1139–1153

18. Bourdin B, Francfort GA, Marigo JJ (2000) Numerical experiments in revisited brittle fracture. J Mech Phys Solids 48:797–826

19. Broberg KB (1999) Cracks and fracture. Academic Press, New York

20. Camanho PP, Davila CG (2002) Mixed-mode decohesion finite elements for the simulation of delamination in composite materials. Technical Report TM-2002-211737, NASA, Hampton, pp 23681–2199

21. Camanho PP, Dávila CG, Moura M (2003) Numerical simulation of mixed-mode progressive delamination in composite materials. J Compos Mater 37(16):1415–1438

22. Chen C, Mangasarian OL (1995) Smoothing methods for convex inequalities and linear complementarity problems. Math Programm 71(1):51–69

23. Chen C, Mangasarian OL (1996) A class of smoothing functions for nonlinear and mixed complementarity problems. Comput Optim Appl 5:97–138

24. Colombo D, Giglio M (2006) A methodology for automatic crack propagation modelling in planar and shell fe models. Eng Fract Mech 73:490–504

25. Dias-da-Costa D, Alfaiate J, Sluys LJ, Júlio E (2009) A discrete strong discontinuity approach. Eng Fract Mech 76(9):1176–1201

26. Erdogan F, Sih GC (1963) On the crack extension in plates under plane loading and transverse shear. J Bas Eng 85:519–527

27. Etse G, Willam K (1999) Failure analysis of elastoviscoplastic material models. J Eng Mech ASCE 125:60–69

28. Hansbo A, Hansbo P (2004) A finite element method for the simulation of strong and weak discontinuities in solid mechanics. Comp Method Appl M 193:3523–3540

29. Kanno Y, Martins JAC (2006) Three-dimensional quasi-static frictional contact by using second-order cone linear complementarity problem. Int J Numer Method Eng 65:62–83

30. Karihaloo BL, Xiao QZ (2003) Modelling of stationary and growing cracks in FE framework without remeshing: a state-of-the-art review. Comput Struct 81:119–129

31. Krueger R (2002) The virtual crack closure technique: history, approach and applications. ICASE CR-2002-211628, NASA

32. Legrain G, Moës N, Verron E (2005) Stress analysis around crack tips in finite strain problems using the extended finite element method. Int J Numer Method Eng 63:290–314

33. Loehnert S, Belytschko T (2007) A multiscale projection method for macro/microcrack simulations. Int J Numer Method Eng 71:1466–1482

34. Ma F, Deng X, Sutton MA, Jr. Newman JC (1999) Mixed-mode crack behavior chapter A CTOD-based mixed-mode fracture criterion. Number STP 1359. ASTM American Society for Testing and Materials, West Conshohocken, pp 86–110

35. Miehe C, Gürses E (2007) A robust algorithm for configurational-force-driven brittle crack propagation with r−adaptive mesh alignment. Int J Numer Method Eng 72:127–155

36. Moës N, Belytschko T (2002) Extended finite element method for cohesive crack growth. Eng Fract Mech 69:813–833

37. Moës N, Dolbow J, Belytschko T (1999) A finite element method for crack growth without remeshing. Int J Numer Method Eng 46:131–150

38. Nocedal J, Wright S (2006) Numerical optimization, series operations research, 2nd edn. Springer, Berlin

39. Oliver J (1989) A consistent characteristic length for smeared cracking models. Int J Numer Method Eng 28:461–474

40. Oliver J (1995) Continuum modelling of strong discontinuities in solid mechanics using damage models. Comput Mech 17:49–61

41. Rabczuk T, Areias P (2006) A meshfree thin shell for arbitrary evolving cracks based on an external enrichment. Comput Model Eng Sci 16(2):115–130

42. Rabczuk T, Areias P, Belytschko T (2007) A meshfree thin shell method for non-linear dynamic fracture. Int J Numer Method Eng 72:524–548

43. Rabczuk T, Belytschko T (2004) Cracking particles: a simplified meshfree method for arbitrary evolving cracks. Int J Numer Method Eng 61:2316–2343

44. Rybicki EF, Kanninen MF (1977) A finite element calculation of stress intensity factors by a modified crack closure integral. Eng Fract Mech 9(4):931–938

45. Schlangen E (1993) Experimental and numerical analysis of fracture processes in concrete. PhD thesis, Delft

46. Schreyer HL, Chen Z (1986) One-dimensional softening with localization. J Appl Mech ASME 53:791–797

47. Sutton MA, Deng X, Ma F, Newman JC Jr, James M (2000) Development and application of a crack tip opening displacement-based mixed mode fracture criterion. Int J Solids Struct 37:3591–3618

48. Teng X, Wierzbicki T (2006) Evaluation of six fracture models in high velocity perforation. Eng Fract Mech 73:1653–1678

49. Van Goethem N, Areias P (2012) A damage-based temperature-dependent model for ductile fracture with finite strains and configurational forces. Int J Fract 178:215

50. Xie M, Gerstle WH (1995) Energy-based cohesive crack propagation modeling. J Eng Mech ASCE 121(12):1349–1358

51. Xie M, Gerstle WH, Rahulkumar P (1995) Energy-based automatic mixed-mode crack-propagation modeling. J Eng Mech ASCE 121(8):914–923